ACS Catalysis

pubs.acs.org/acscatalysis

Research Article

Fe-MOF Materials as Precursors for the Catalytic Dehydrogenation of Isobutane

Alberto Rodriguez-Gomez, Samy Ould-Chikh, Javier Castells-Gil, Antonio Aguilar-Tapia, Pierre Bordet, Mogbel A. Alrushaid, Carlos Marti-Gastaldo, and Jorge Gascon*

Cite This: *ACS Catal.* 2022, 12, 3832−3844

Read Online

ACCESS | Metrics & More | Article Recommendations | Supporting Information

ABSTRACT: We investigate the use of a series of iron-based metal−organic frameworks as precursors for the manufacturing of isobutane dehydrogenation catalysts. Both the as-prepared and spent catalysts were characterized by PXRD, XPS, PDF, ICP-OES, and CHNS+O to determine the physicochemical properties of the materials and the active phases responsible for the catalytic activity. In contrast to the previous literature, our results indicate that (i) the formation of metallic Fe under reaction conditions results in secondary cracking and coke formation; (ii) the formation of iron carbide only contributes to coke formation; and (iii) the stabilization of the Fe^{2+} species is paramount to achieve stable and selective catalysts. In this sense, promotion with potassium and incorporation of titanium improve the catalytic performance. While potassium is well known to improve the selectivity in iron-catalyzed dehydrogenation reactions, the unprecedented effect of titanium in the stabilization of a nanometric titanomaghemite phase, even under reductive reaction conditions, results in a moderately active and highly selective catalyst for several hours on stream with a remarkable resistance to coke formation.

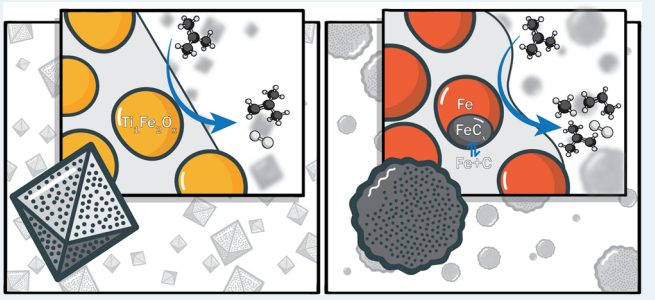

KEYWORDS: *iron catalysts, MOF structures, dehydrogenation of alkanes, XPS, in situ TEM*

INTRODUCTION

The growing demand for light olefins has overtaken the capacity of the current naphtha steam crackering, a process through which these important chemical intermediates have been traditionally produced. This has spurred intensive research into new technologies to fill this demand gap. In this spirit, high-severity fluid catalytic cracking (FCC) processes that maximize short olefin productivity along with other on-purpose processes have been developed.[1−3] One outstanding example of the latter is the production of butylenes, where nonoxidative dehydrogenation of isobutane is currently used to cover the demand for isobutylene, which is employed as a precursor of high-octane oxygenates (MTBE and ETBE) and in the production of butyl rubber.[4] As for the oxidative route with di-oxygen, despite favorable from a thermodynamic and kinetic point of view, has disadvantages such as the low selectivities obtained so far or the high exothermicity and risk of formation of explosive atmospheres.[4,5] Commercial catalysts, based on platinum or chromium, usually promoted with tin and alkali metals, respectively, have shown the best catalytic performance.[6,7] However, the high cost of platinum and the toxicity of chromium (Cr^{6+} species) have encouraged the search for alternatives such as vanadium[8−11] and, to a lesser extent, molybdenum,[12,13] zirconium,[14,15] gallium,[16,17] indium,[18] and iron oxides,[19−23] which have all shown some promise as potential active phases. Among them, Fe is especially interesting because of its natural abundance, low cost, and low toxicity.

The nature of the active sites in iron-based dehydrogenation catalysts is a matter of debate. Indeed, Fe generally exhibits multiple oxidation states under alkane dehydrogenation reaction conditions. Lobo et al.[24] claimed that isolated Fe^{3+} species on an Fe-ZSM-5 catalyst are the preferred site for adsorption of propane, which is then dehydrogenated following a redox cycle involving Fe^{3+}/Fe^{2+} species. Similarly, octahedral Fe^{2+} sites in an ordered mesoporous Al_2O_3 promoted with a ZnO matrix have been shown to be highly active in the dehydrogenation of isobutane, presenting conversions of isobutane of above 40% at 580 °C and a moderate selectivity to isobutylene in the 70−85% range.[21] In a fundamental study, Hu et al. reported that isolated species are the most active and selective for the dehydrogenation of propane at 650 °C at low conversions, while iron oxide clusters are poorly active for the reaction. On the other hand, metallic

Received: November 18, 2021
Revised: February 13, 2022
Published: March 14, 2022

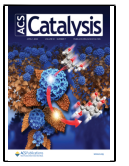

Table 1. Specific BET Surface Area, Elemental Analysis by ICP and CHNS+O, and Average Crystallite Size by the Scherrer Equation for the Different Fresh Catalytic Systems

	[a]	[b]	ICP and CHNS+O/at. %						XRD crystallite size[c]/nm		
catalyst	S_{BET}[a]/$m^2 \cdot g^{-1}$	V_T[b]/$cm^3 \cdot g^{-1}$	Fe	Ti, K	C	O	N	H	γ-Fe_2O_3	α-Fe	Fe_3C
Fe/C_{BTC}	257	0.27	11.1	0	46.9	17.6	0.2	24.2	4.9	55	21
$K/Fe/C_{BTC}$	256	0.28	11.2	0.7 (K)	46.1	17.5	0.2	24.3	5.2	40	20
$Fe/C_{MIL\text{-}100}$	214	0.15	13.2	0	45.4	17.8	0.1	23.5	n.d.	98	65
$TiFe/C_{MUV\text{-}101}$	263	0.19	9.2	5.5 (Ti)	34.5	25.2	0.7	24.9	4.5	48	n.d.

[a]S_{BET} is the total surface calculated by the BET method and applying the Rouquerol approach for micropore materials. [b]V_T is the total pore volume estimated from a single-point measurement at P/P_0 = 0.94 of the N_2 adsorption isotherm. [c]Calculated by applying the Scherrer equation.

iron presents an order of magnitude higher activity in the conversion of propane but with a very low selectivity to propylene.[19] Shimada et al. studied the dehydrogenation of isobutane on iron-loaded activated carbons and concluded that magnetite is the main catalytic phase. The addition of CO_2 to the feed helped to keep the active Fe_3O_4 phase present through a redox cycle with metallic iron.[25] In the same line, Stobbe, Boot, and co-workers pointed that the stabilization of Fe_3O_4 over zirconia or magnesia supports improved the selectivity toward dehydrogenation products, while the formation of metallic iron resulted in carbon nucleation and catalyst deactivation.[26,27] In fact, it is well known that metallic iron is not active for dehydrogenation but for the cleavage of C−C bonds and other secondary reactions such as hydrogenolysis.[13,16,20] Moreover, in the presence of hydrocarbons, it rapidly forms iron carbide, which is inactive for dehydrogenation and also promotes coke (graphite) formation.[28]

Over the last decade, the use of metal−organic frameworks (MOFs) as catalyst precursors has gained momentum due to the unique dispersion achievable via pyrolysis,[29] calcination,[30] or even electroreduction[31] of these hybrid materials. MOFs can provide highly dispersed metal or metal oxide clusters within hierarchical pores and unprecedented physicochemical properties, at least by conventional synthesis methods.[32] In particular, these properties may be of special interest in dehydrogenation reactions over metal oxides (Cr, V, Ga, Fe, etc.) as they generally require high dispersion of the active phase and the presence of low-coordination metal sites.[6] In 2018, Jones et al. reported the use of Fe-MOF as a precursor for the synthesis of propane dehydrogenation catalysts.[23] Despite working at low partial pressures of propane, it sets a precedent for the potential of well-dispersed iron nanoparticles supported in carbon for dehydrogenation reactions, not only propane but also ethane or butanes, especially the latter due to the lower thermodynamic limitations. On the other hand, common supports such as silica or zeolites require the use of sophisticated techniques such as organometallic synthesis or particularly stringent sol−gel conditions to obtain isolated or low-coordination iron oxide sites.[19,24] In this work, we further explore the potential application of Fe-MOF as catalyst precursors for the nonoxidative dehydrogenation of isobutane and unravel important parameters determining catalyst stability and selectivity. In addition to studying different Fe-based MOFs as precursors, we demonstrate that both the promotion with K and the incorporation of Ti into the active iron phase improve the catalytic performance. While potassium is known to improve the selectivity in dehydrogenation of alkanes by poisoning undesired acid sites, titanium has shown to stabilize the oxidized state of iron via the formation of a titanomaghemite phase,[33] which, based on its Ellingham diagram, confers a high resistance to chemical reduction. Overall and in contrast to earlier work, our results indicate that (i) the formation of metallic Fe under reaction conditions results in secondary cracking and coke formation; (ii) the formation of iron carbide only contributes to coke formation; and (iii) the stabilization of Fe^{2+} species is paramount to achieve stable and selective catalytic behavior.[23]

MATERIALS AND METHODS

Catalyst Preparation. A series of MOF materials were used as catalyst precursors. According to a previously reported protocol,[33] MIL-100(Fe) was synthesized in a Schott glass jar containing 3.4 g of trimesic acid (98%, TCI Europe) and 9.72 g of $FeCl_3 \cdot 6H_2O$ (99%, Sigma-Aldrich) and 120 mL of H_2O. The solution was heated at 130 °C for 72 h, yielding an orange microcrystalline powder. The solid was washed with copious amounts of water and methanol (99.8%, Sigma-Aldrich) before being further purified by Soxhlet extraction with hot methanol overnight. Finally, the solid was dried at room temperature under dynamic vacuum. MUV-101(Fe, Ti) was synthesized in a Schott glass jar containing 1.25 g of trimesic acid (98%, TCI Europe) dissolved in a mixture of 120 mL of anhydrous DMF (99.8%, Sigma-Aldrich) and 70 mL of glacial acetic acid (99.7%, Sigma-Aldrich) thoroughly bubbled with argon before the addition of 370 μL of $Ti(OiPr)_4$ (97%, Sigma-Aldrich) and 305 mg of anhydrous $FeCl_2$ (99%, Sigma-Aldrich). The clear solution was heated at 120 °C for 48 h to yield a dark-brown microcrystalline solid. The solid was separated by centrifugation (5000 rpm) and thoroughly washed with fresh DMF (3 × 50 mL) and methanol (3 × 50 mL). The solid was further purified by Soxhlet extraction with hot methanol overnight and allowed to dry at room temperature under dynamic vacuum. Commercial Fe-BTC (Basolite F-300) was purchased from Sigma-Aldrich.

The (Ti/K)Fe/C catalysts were obtained by pyrolysis of 3.0 g of the listed MOF precursors at 600 °C for 8 h using a 25 $mL \cdot min^{-1}$ N_2 flow and a heating ramp of 2 $°C \cdot min^{-1}$. Taking into account the pyrophoric nature of the resulted materials, all samples were passivated in a mixture of 2% O_2/N_2 during 2 h at room temperature before being exposed to air. As seen below (Table 1, elemental analysis), this treatment results in the incorporation of a certain amount of nitrogen into the material, presumably from traces of DMF used as a solvent for synthesis. The pyrolyzed and passivated materials were labeled as $Fe/C_{MIL\text{-}100}$, $TiFe/C_{MUV\text{-}101}$, and Fe/C_{BTC}. K-promotion was carried out by incipient wetness impregnation with a 0.26 M potassium carbonate solution in methanol/water [1:1] for a nominal potassium content of 2 wt % ($K/Fe/C_{BTC}$). Finally, nonsupported commercial Fe_2O_3 (<30 nm, Sigma-Aldrich) and TiO_2 (<25 nm, Sigma-Aldrich) were used as reference materials.

https://doi.org/10.1021/acscatal.1c05303
ACS Catal. 2022, 12, 3832−3844

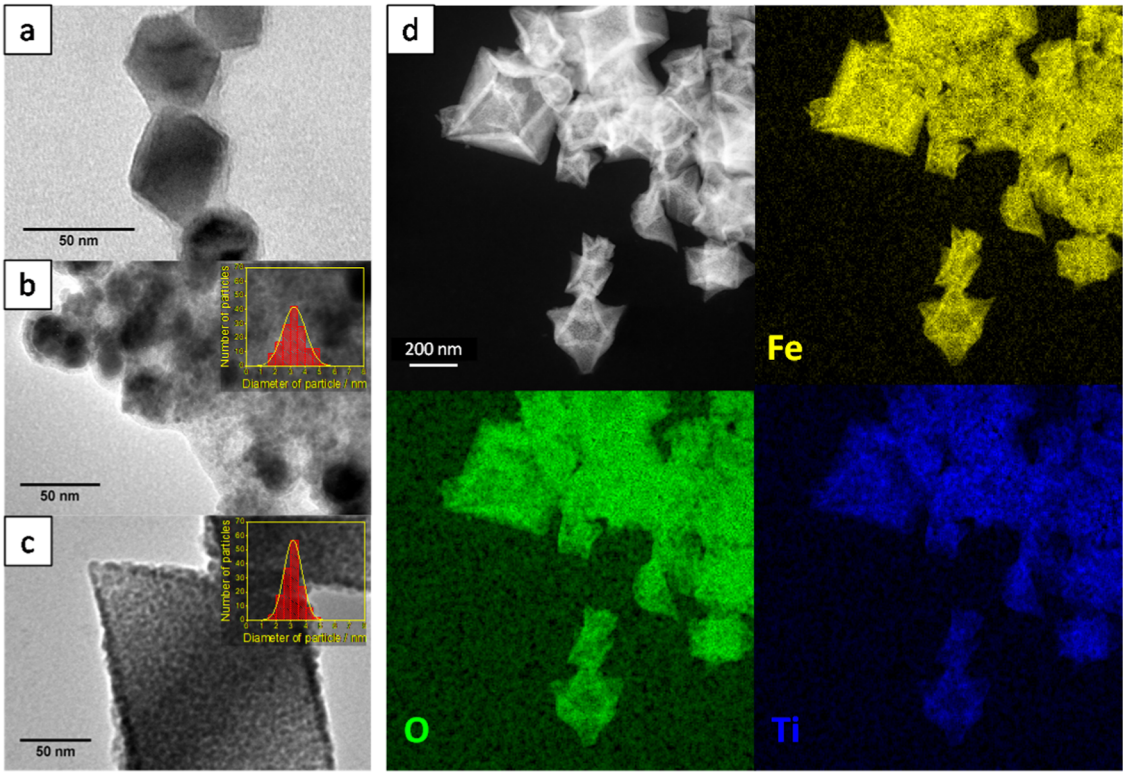

Figure 1. TEM images and size distribution histograms for pyrolyzed Fe/$C_{MIL\text{-}100}$ (a), Fe/C_{BTC} (b), and TiFe/$C_{MUV\text{-}101}$ (c), a survey image of an octahedral corner used for STEM-EELS characterization (d) with the individual Fe (yellow), Ti (blue), and O (green) chemical maps built, respectively, with Fe and Ti L-edges and O K-edge.

X-ray Photoelectron Spectroscopy (XPS). The as-prepared catalysts were analyzed in a Kratos Axis Ultra DLD spectrometer equipped with a monochromatic Al Kα X-ray source ($h\nu$ = 1486.6 eV) operating at 150 W, a multichannel plate, and a delay line detector under a vacuum of 1×10^{-9} Torr. Measurements were performed in the hybrid mode using electrostatic and magnetic lenses, and the take-off angle (angle between the sample surface normal and the electron optical axis of the spectrometer) was 0°. All spectra were recorded using an aperture slot of 300×700 μm^2. The survey and high-resolution spectra were collected at fixed analyzer pass energies of 160 and 20 eV, respectively. Samples were mounted in the floating mode to avoid differential charging. Charge neutralization was required for all samples. Binding energies were referenced to the sp^2-hybridized (C═C) carbon for the C 1s peak set at 284.4 eV. Prereduced and spent catalysts were mounted on the holder in a glovebox under a controlled environment (argon) and then transferred to the XPS instrument using a transfer vessel for air-sensitive samples.

***In Situ* Transmission Electron Microscopy (*In Situ* TEM).** Transmission electron microscopy was performed using a Cs-corrected FEI Titan electron microscope operated at 300 kV. MUV-101(Fe, Ti) NPs were dispersed in ethanol and drop-deposited on a silicon-based microelectromechanical system (MEMS) chip from DENSsolutions. After loading the sample, the MEMS chip was used without further plasma cleaning, assembled into the DENSsolutions Climate holder, and heated in the microscope at 130 °C for 2 h under N_2 (1 bar). The sample was heated up to 600 °C at 2 °C·min^{-1} under N_2 (1 bar) to decompose the MOF into a mixture of titanomaghemite and carbon. Then, the sample was cooled down to room temperature, and the atmosphere was switched with a flow of 4% H_2/Ar and a pressure of 1 bar. The sample was then heated back to a temperature of 600 °C using a ramp of 5 °C·min^{-1}, and the latter temperature was maintained until no structural change was further observed.

Temperature-Programmed Reduction (TPR). All measurements were conducted in an Altamira AMI-200 instrument. After a pretreatment in helium at 100 °C, the sample was cooled down to 60 °C and then submitted to a treatment in 4% H_2/Ar until 600 °C using a heating ramp of 10 °C·min^{-1}. The gas mixture evolution was followed by mass spectrometry (m/z = 2, m/z = 15, m/z = 18, m/z = 28, and m/z = 44). Commercial Fe_2O_3 nanoparticles ($Ø_{av}$ = 30 nm) were used to quantify the hydrogen consumption in each experiment.

Catalyst Evaluation. Catalytic performance in the non-oxidative dehydrogenation of isobutane was tested at atmospheric pressure in a tubular quartz reactor (Ø = 8 mm) in the fixed-bed mode. Typically, 200 mg of the pyrolyzed, passivated, and sized catalyst (150−250 μm) was loaded in the reactor and submitted to 50 mL·min^{-1} 4% H_2/Ar flow at 600 °C using a heating ramp of 10 °C·min^{-1} (for a fairer comparison, the reference measurement with commercial nonsupported Fe_2O_3 and TiO_2 nanoparticles was performed using 100 mg, which is close to the metal content in the pyrolyzed MOFs). Next, the catalyst was cooled down until reaction temperature, 550 °C, in an argon flow and kept during 10 min at this temperature before feeding the reaction mixture, 4 mL·min^{-1} of equimolar iC_4H_{10}/N_2. The catalyst was tested during 540 min and kept under an argon atmosphere during the cooling step. The reactant and products were analyzed online by gas chromatography conducted on a Varian 450-GC gas chromatograph with a Molsieve 13X column equipped with a TCD for the analysis of N_2 and a HP-Alumina/KCl column

https://doi.org/10.1021/acscatal.1c05303
ACS Catal. 2022, 12, 3832−3844

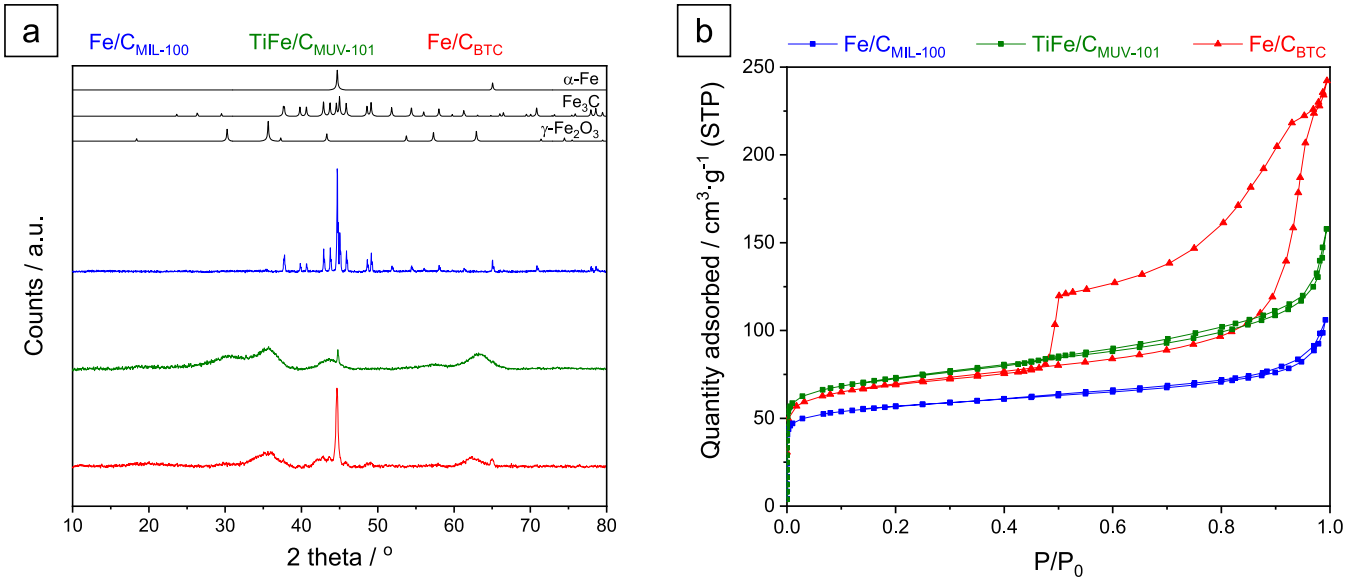

Figure 2. PXRD patterns (a) and N_2 adsorption/desorption isotherms (b) of the pyrolyzed and passivated samples: Fe/C_{BTC} (red), TiFe/$C_{MUV-101}$ (green), and Fe/$C_{MIL-100}$ (blue).

equipped with a FID for the analysis of hydrocarbons. N_2 concentration was used as an internal standard. The conversion of isobutane, selectivity to hydrocarbons, and carbon balance in the gas phase were calculated using the following equations

$$iC_4H_{10}\ \text{conversion}\ (\%) = 100 - \frac{[iC_4H_{10}]_{out}}{[iC_4H_{10}]_{in}}\frac{[N_2]_{in}}{[N_2]_{out}} \times 100$$

$$\text{selectivity to } C_xH_y(\%) = \frac{x[C_xH_y]}{\sum x[C_xH_y]} \times 100$$

C_xH_y = hydrocarbon product

x = number of carbon atoms
y = number of hydrogen atoms

$$\text{carbon balance in gas phase}\ (\%) = \frac{\sum x[C_xH_y]_{out}}{[iC_4H_{10}]_{in}}\frac{[N_2]_{in}}{[N_2]_{out}} \times 100$$

RESULTS AND DISCUSSION

Characterization of the As-Prepared Catalysts. The pyrolyzed and passivated Fe/C samples were imaged by TEM, revealing clear textural and morphological differences, as shown in Figure 1: while Fe/$C_{MIL-100}$ is mostly characterized by large pseudo-octahedral structures in a wide range of particle sizes of around 30−100 nm (Figure 1a), Fe/C_{BTC} exhibits a highly dispersed iron phase embedded in the carbon matrix with a narrow particle size distribution averaging 3.5 nm diameter but also presenting some larger aggregates (Figure 1b), in agreement with previous reports.[34,35] On the other hand, the bimetallic iron−titanium sample (Figure 1c), obtained from the pyrolysis of the MUV-101(Fe, Ti) MOF, isoreticular to MIL-100 but built from bimetallic $TiFe_2$ metal-oxo clusters,[33,36] shows similar pseudo-octahedral mesotructures but composed of highly dispersed and homogeneously distributed metal (oxide) nanoparticles with a diameter in the 2−4 nm range. Elemental analysis by STEM-EELS of the nanoparticle arrays (Figure 1d) shows a homogeneous distribution of Fe (yellow), O (green), and Ti (blue).

The main physicochemical properties of the catalysts, including the elemental composition, BET surface area, total pore volume, and estimated particle size for different crystal phases, are summarized in Table 1. The metal content is in the 11−15 at. % range for all samples, with higher oxygen-to-metal and metal-to-carbon ratios in the bimetallic TiFe/$C_{MUV-101}$, which may indicate a higher oxidation (lower carburization) degree of this catalyst. The PXRD patterns (Figure 2a) show different compositions in metal oxide, metallic iron, and iron carbide depending on the precursor. For instance, Fe/$C_{MIL-100}$ exhibits mainly sharp peaks corresponding to a cementite-type iron carbide phase (Fe_3C), with an estimated average crystallite size of 65 nm by applying the Scherrer equation. On the other hand, (K)Fe/C_{BTC} and TiFe/$C_{MUV-101}$ show broad peaks at 30.2, 35.6, 43.3, and 62.9° attributable to a highly dispersed maghemite-type phase with an average crystallite size of 4.5 nm, slightly higher than the value estimated by microscopy for the homogeneously distributed nanoparticles (see histograms in Figure 1). In addition, the (K)Fe/C_{BTC} samples show diffraction peaks associated with Fe_3C and a sharp peak at 44.7° characteristic of metallic iron. To a lesser extent, the latter is also present in TiFe/$C_{MUV-101}$, while iron carbide is absent. Our previous structural analysis considering the pair distribution functions (PDFs) has demonstrated that the pyrolysis of the MUV-101 MOF leads to a highly defective titanomaghemite phase.[33] The latter experimental atomic pair distribution function is redrawn in the Supporting Information to facilitate the comparison with the subsequent evolution of the TiFe/$C_{MUV-101}$ catalyst (*vide infra*). With regard to textural properties, N_2 adsorption/desorption isotherms of the pyrolyzed samples (Figure 2b) exhibit clear differences: (i) Fe/$C_{MIL-100}$ and TiFe/$C_{MUV-101}$ show the typical isotherm of a microporous material with a slight contribution of mesopores, which results in a specific surface area of around 214 and 263 $m^2 \cdot g^{-1}$ and pore volume of 0.15 and 0.19 $cm^3 \cdot g^{-1}$, respectively, and (ii) (K)Fe/C_{BTC}

https://doi.org/10.1021/acscatal.1c05303
ACS Catal. 2022, 12, 3832−3844

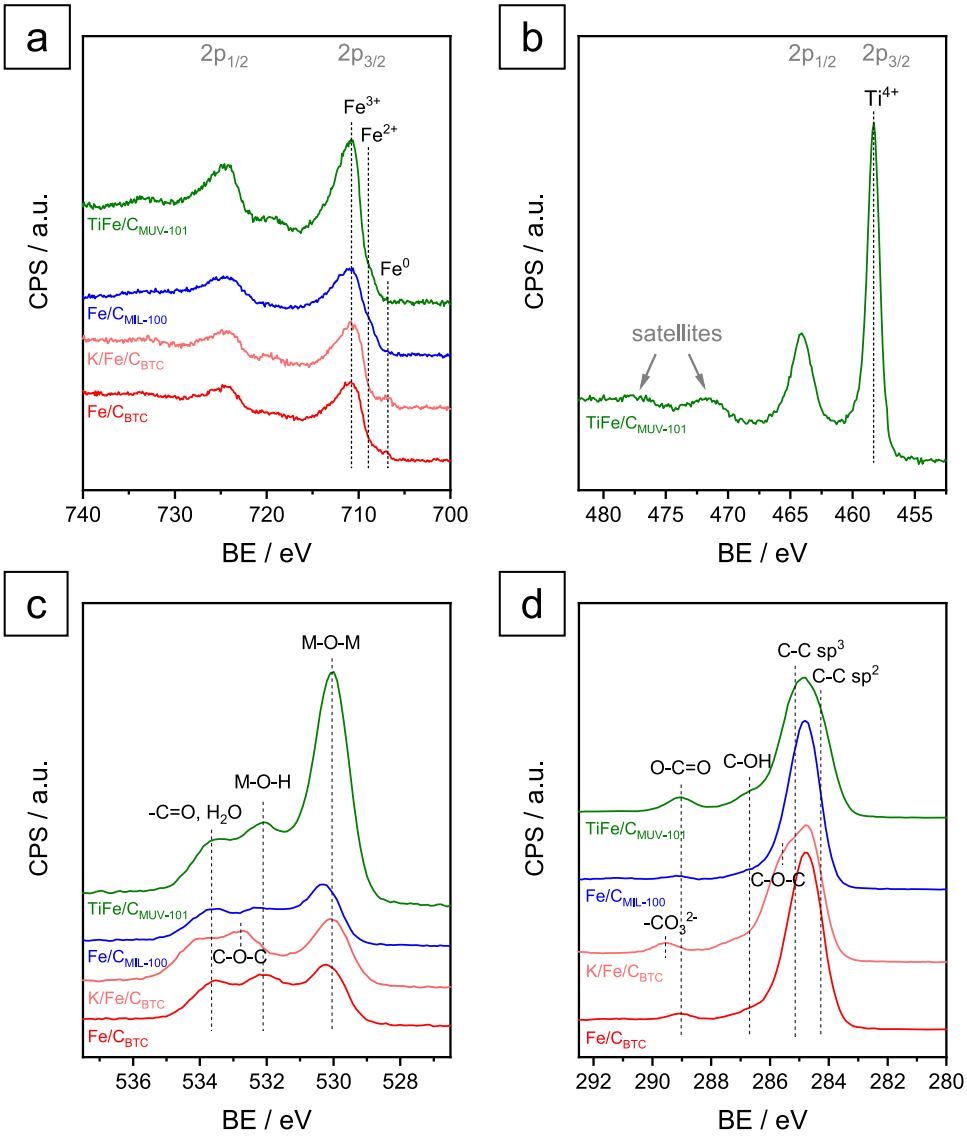

Figure 3. XPS spectra in the Fe 2p (a), Ti 2p (b), O 1s (c), and C 1s (d) regions for the different pyrolyzed and passivated catalysts: Fe/C_{BTC} (red), $K/Fe/C_{BTC}$ (pale red), $Fe/C_{MIL\text{-}100}$ (blue), and $TiFe/C_{MUV\text{-}101}$ (green).

displays a hysteresis loop at P/P_0 above 0.45 typical of mesoporous cavities communicated by windows smaller than 3.5 nm[37] and a high microporosity derived from the high nitrogen uptake at very low relative pressure, resulting in ca. 257 $m^2 \cdot g^{-1}$ and 0.27 $cm^3 \cdot g^{-1}$ specific surface area and total pore volume, respectively. Moreover, the micropore volume is ca. 0.05−0.06 in all cases (see Table S1), which may be associated with the carbon matrix. On the other hand, V_{micro}/V_{meso} values of 0.29, 0.27, 0.71, and 0.5 in Fe/C_{BTC}, $K/Fe/C_{BTC}$, $Fe/C_{MIL\text{-}100}$, and $TiFe/C_{MUV\text{-}101}$, respectively, evidence the higher contribution of mesopores in $(K)Fe/C_{BTC}$, presumably conferred by the interstitial voids in between metal oxide nanoparticles. The less-hierarchical structure of both $Fe/C_{MIL\text{-}100}$ and $TiFe/C_{MUV\text{-}101}$ catalysts, given by ordered pseudo-octaedral particles, could explain the lower mesoporosity, especially in the case of $Fe/C_{MIL\text{-}100}$, with the highest V_{micro}/V_{meso} ratio and in the absence of metal oxide nanoparticles (see TEM images of Figure 1).

Next, the surface chemical state of the catalysts has been analyzed by XPS (Figure 3). In all cases, a main peak centered at 710.8 ± 0.2 eV ($2p_{3/2}$, see Figure 3a) indicates the presence of $Fe_2^{3+}O_3$,[38−40] confirmed by its satellite at 719.5 eV. Both $Fe/C_{MIL\text{-}100}$ and $TiFe/C_{MUV\text{-}101}$ present a second component, to a lower extent, centered at around 709.4 eV, which may be associated with Fe^{2+}.[35,36] This could explain the less-clear feature of the satellite peak. On the other hand, $(K)Fe/C_{BTC}$ samples exhibit a small peak at 706.9 eV typical of metallic iron or iron carbide.[40,41] It is worth noting the higher relative area of the Fe 2p signal in $TiFe/C_{MUV\text{-}101}$ considering its lower Fe at. %, which suggests a higher exposure of surface Fe sites. Moreover, the Ti 2p signal (Figure 3b) shows two sharp peaks centered at 458.3 and 464.1 eV, associated to the $2p_{3/2}$ and $2p_{1/2}$ components, respectively, and two satellite peaks at 471.7 and 477.0 eV.[42] The values of 458.3 eV for Ti $2p_{3/2}$ BE and 5.8 eV for split spin-orbit energy are slightly different from the expected ones for Ti^{4+} (458.7 ± 0.2 and 5.7 ± 0.08 eV, respectively) but far from those for Ti^{3+}.[43] This red shift in binding energy has been attributed to the presence of Fe−O−Ti bonds by other authors.[44−46] In addition, the O 1s spectrum (Figure 3c) shows the presence of peaks at ca. 530.0, 532.1, and 533.7 eV associated to M−O−M, M−OH, and −C═O (or H_2O) species, respectively.[33] The higher relative intensity

https://doi.org/10.1021/acscatal.1c05303
ACS Catal. 2022, 12, 3832−3844

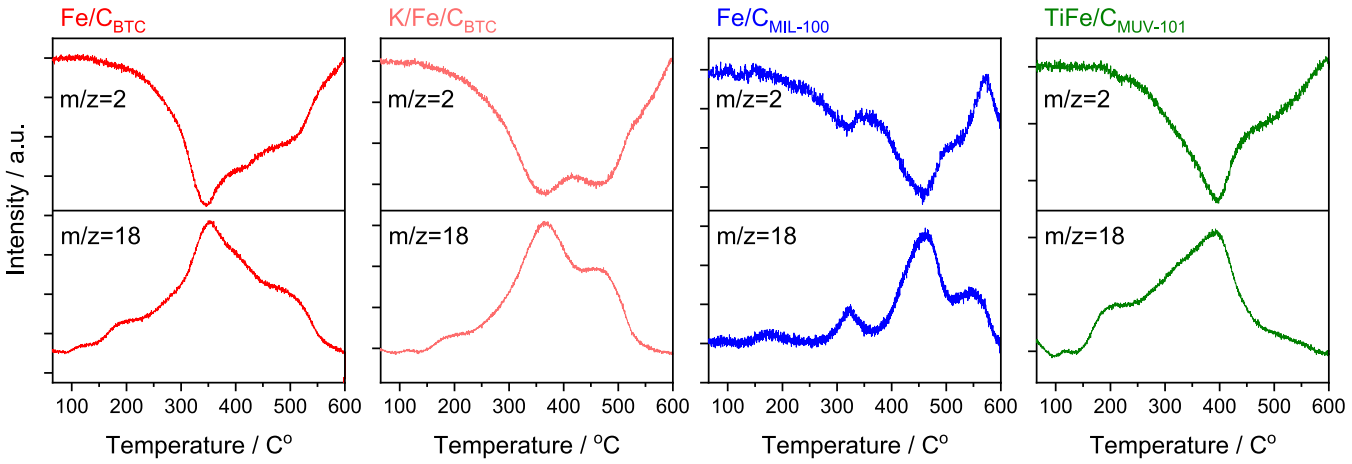

Figure 4. Temperature-programmed reduction (H_2-TPR) profile of the as-prepared catalysts recorded by mass spectrometry. m/z values of 2 and 18 were used to follow the evolution of hydrogen and water, respectively. Fe/C_{BTC} (red), K/Fe/C_{BTC} (pale red), Fe/$C_{MIL-100}$ (blue), and TiFe/$C_{MUV-101}$ (green).

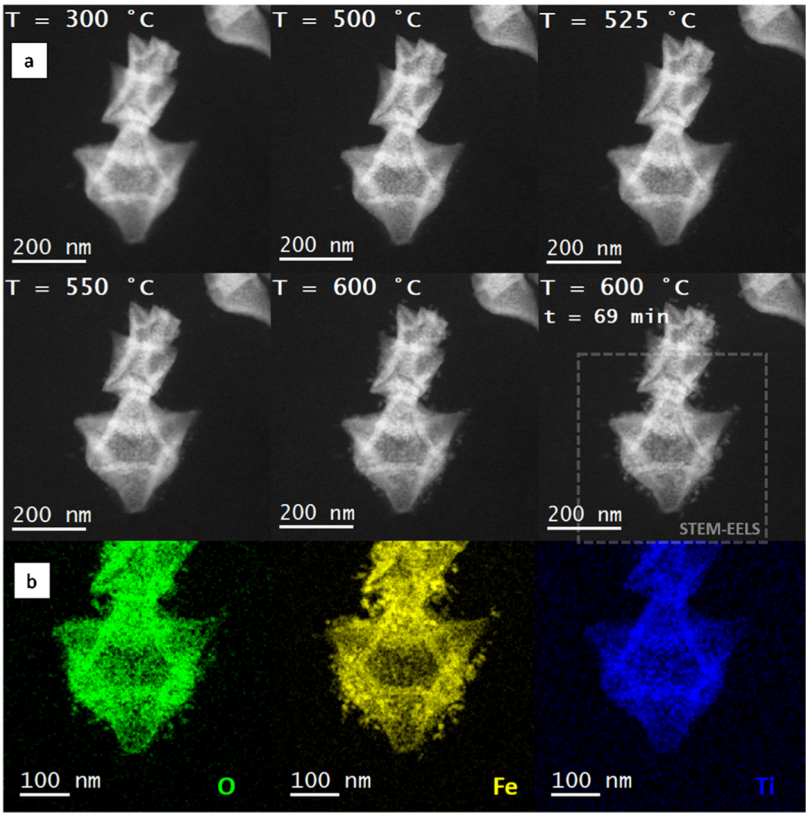

Figure 5. *In situ* ADF-STEM imaging of the TiFe/$C_{MUV-101}$ catalyst during reduction treatment. Temperature ranged from 300 to 600 °C under 1 bar 4% H_2 in argon. (a) Only selected temperatures are shown. (b) STEM-EELS characterization showing the individual Fe (yellow), Ti (blue), and O (green) chemical maps built, respectively, with Ti and Fe L-edges and O K-edge.

of the M−O−M component in TiFe/$C_{MUV-101}$ indicates a greater presence of metal oxide on the surface. On the other hand, the C 1s signal (Figure 3d) for all samples shows a main component at ca. 284.8 eV of C−C species, which can be split into two components at 284.3 and 285.2 eV of sp^2 and sp^3 hybridization, respectively.[33] Additionally, alcohol, carboxylic, and other oxygenated species, most likely remnants of the thermal decomposition of the linker (trimesic acid) during pyrolysis, can be detected (see more details in Figure S1 and Table S2). In this sense, the promotion with potassium results in a higher oxidation degree of carbon, with the appearance of carbonate and ester peaks at 285.6 and 289.5 eV, respectively, not detectable in the starting Fe/C_{BTC} material.

Study of the Catalysts Subjected to a Prereduction Treatment. The reducibility of the pyrolyzed systems has been followed by temperature-programmed reduction measurements (TPR). Since not only metal reduction but also the hydrogenation and/or partial decomposition of the carbon support is expected during the hydrogen treatment, mass measurements for hydrogen, methane, carbon monoxide, carbon dioxide, and water were recorded (m/z = 2, 15, 28, 44, and 18, respectively). All reduction profiles (Figure 4)

https://doi.org/10.1021/acscatal.1c05303
ACS Catal. 2022, 12, 3832−3844

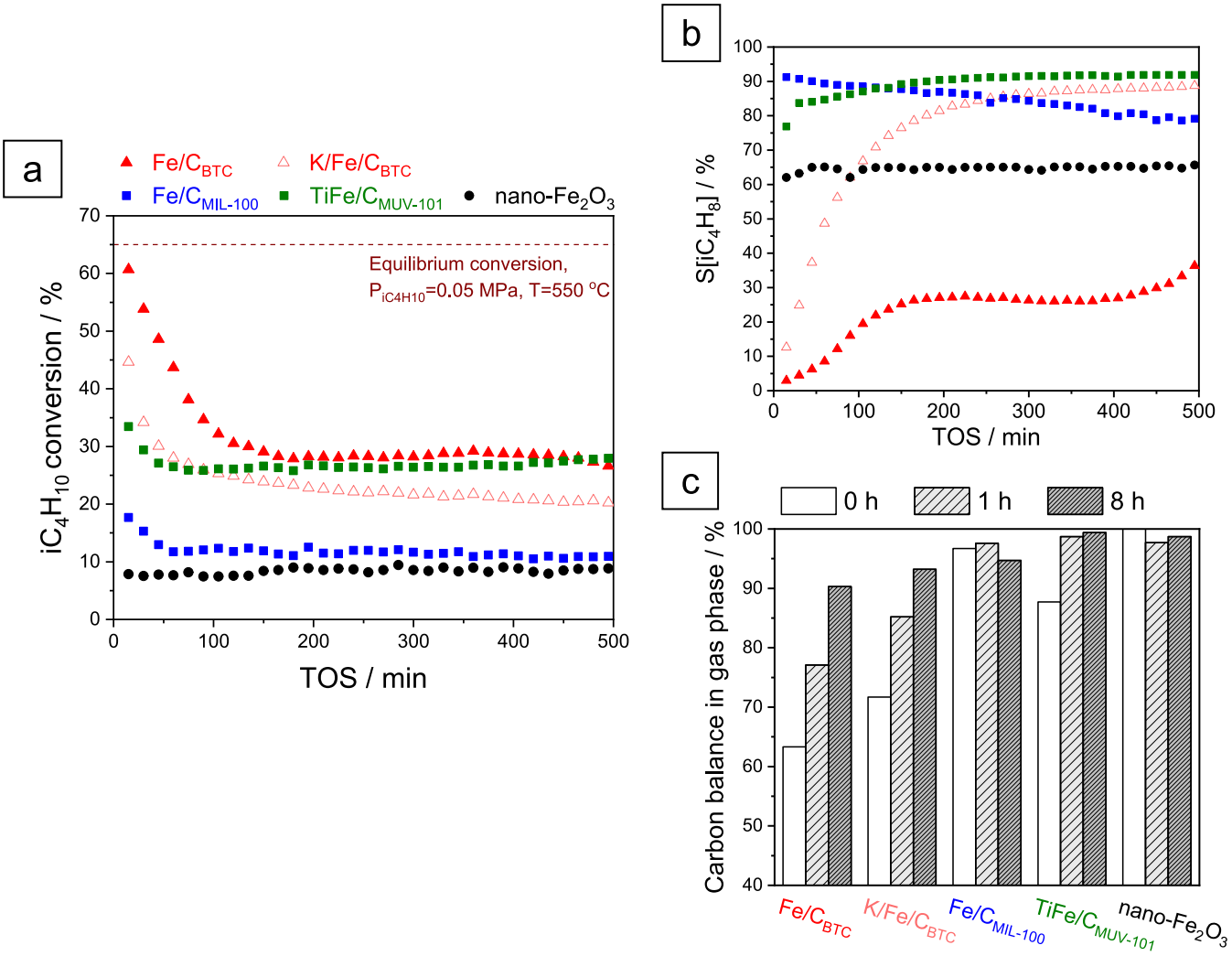

Figure 6. Catalytic performance of the Fe-based catalytic systems: isobutane conversion (a), selectivity to isobutylene (b), and carbon balance (c) in the gas phase. Fe/C_{BTC} (red), $K/Fe/C_{BTC}$ (pale red), $Fe/C_{MIL\text{-}100}$ (blue), and $TiFe/C_{MUV\text{-}101}$ (green).

display (i) a first peak at a temperature of below 200 °C, associated with the desorption of water trapped inside the porous structure; (ii) a broad (complex) peak in the 300−450 °C range, presumably due to the reduction of maghemite to magnetite and FeO, as exemplified by the case of $Fe/C_{MIL\text{-}100}$ with two well-separated peaks with maxima at 320 and 450 °C; and (iii) a peak above 450 °C associated with the formation of Fe^0. In particular, the latter is less significant for $TiFe/C_{MUV\text{-}101}$. A rough estimation of the total hydrogen consumption from the mass spectra (see Table S3) shows ca. half the hydrogen consumption in the case of $TiFe/C_{MUV\text{-}101}$ compared to $(K/)Fe/C_{BTC}$ (ca. 14.8 and 20.8−21.7 $mmol{\cdot}g_{Fe}^{-1}$, respectively). However, other reactions in which hydrogen could be involved must be taken into account. In fact, at high temperatures (ca. 500 °C), carbon monoxide is observed (m/z = 28, see Figure S2), meaning that part of the carbon matrix is decomposing in the presence of hydrogen. The peak intensity associated with this molecule is relatively higher in $Fe/C_{MIL\text{-}100}$, which shows 6.1 $mmol{\cdot}g^{-1}$ hydrogen consumption. Second, carbon dioxide and methane (m/z = 44 and m/z = 15, respectively) have also been detected, although to a minor extent. The effect of both reduction and decomposition processes in the catalysts was analyzed by TGA in the presence of a 4% H_2/Ar flow (see Figure S3). It can be seen that ca. 10 wt % starting material is lost at 500 °C, after trapped water desorption and metal reduction, as deduced from the TPR profile (Figure 4), while 6 wt % is gone in the 500−600 °C range at the expense of mainly carbon monoxide.

The structural changes during the reduction treatment (4% H_2/Ar) of the $TiFe/C_{MUV\text{-}101}$ catalyst were followed by *in situ* TEM (Figures 5 and S4) from room temperature (RT) up to 600 °C. There were no significant morphological and textural changes until 500 °C. Above this temperature, some nanoparticles began to nucleate on the surface of the pseudo-octahedral aggregates. This phenomenon was intensified when the temperature was increased to 600 °C. Maintaining the temperature at 600 °C also resulted in the growth and aggregation of newly formed nanoparticles, whose size stabilized after 69 min (10−15 nm). The elemental composition highlighted by STEM-EELS analysis revealed the presence of only iron and oxygen atoms in these particles (Figure 5b). This clearly indicates an exsolution of a reduced FeO_x phase originating from the titanomaghemite nanoparticles (see Figure S4b). *A fortiori* the Fe/Ti molar ratio of the titanomaghemite phase must necessarily decrease from its initial value of ∼2. Interestingly, there is also a ∼100 °C difference between the maximum consumption of hydrogen

https://doi.org/10.1021/acscatal.1c05303
ACS Catal. 2022, 12, 3832−3844

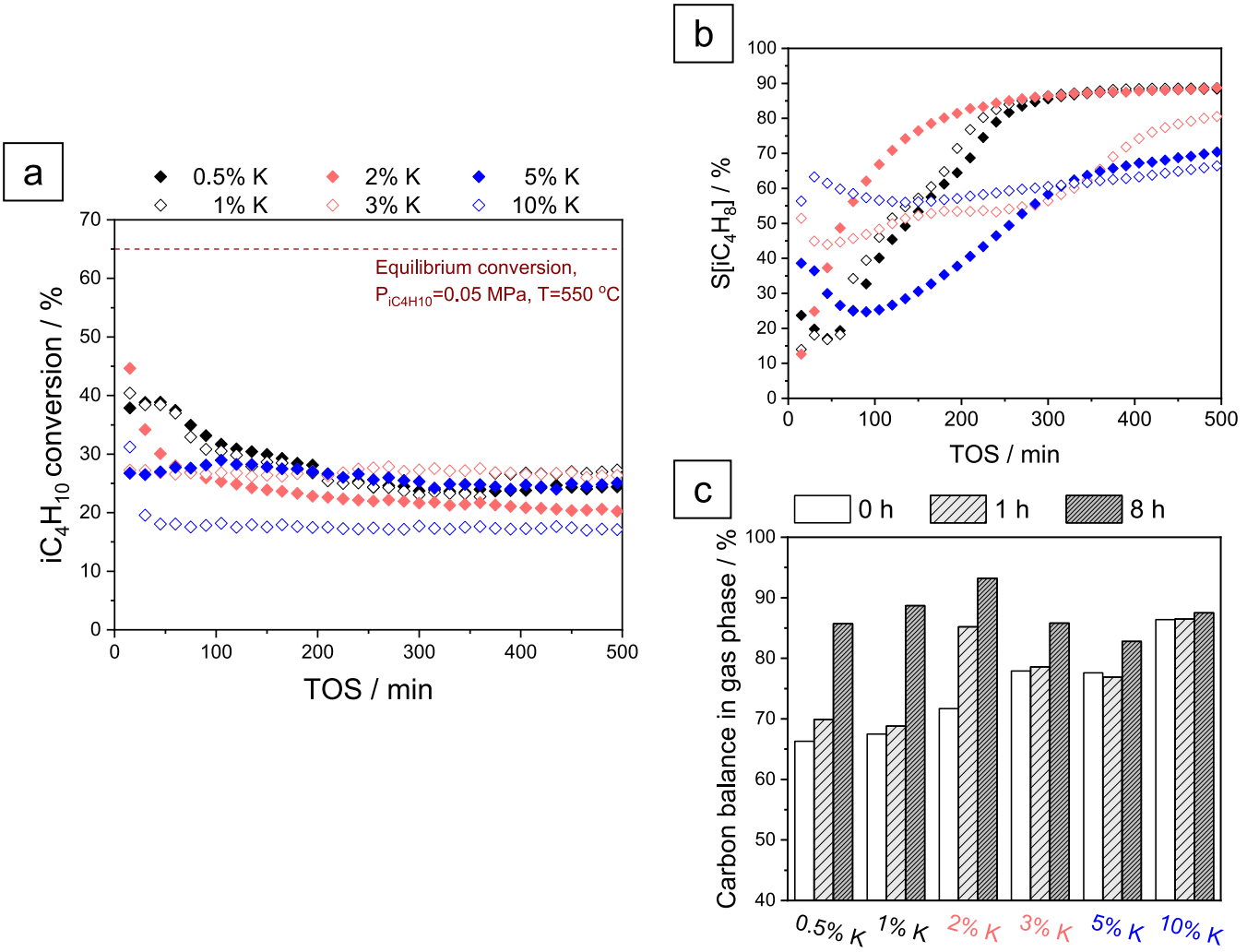

Figure 7. Catalytic performance of the K-promoted Fe/C_{BTC} catalysts: isobutane conversion (a), selectivity to isobutylene (b), and carbon balance (c) in the gas phase.

observed by H_2-TPR and the appearance of nanoparticles imaged by TEM. This would suggest that the nucleation rate of the reduced FeO_x nanoparticles is limited by atom diffusion going from the bulk of the aggregate to its surface.

Finally, the PXRD patterns of the prereduced catalysts (Figure S5) show the prevalence of metallic iron in Fe/C_{BTC}, K/Fe/C_{BTC}, and Fe/$C_{MIL\text{-}100}$ and the presence of iron carbide (Fe_3C) to a lower extent in the latter. In the TiFe/$C_{MUV\text{-}101}$ catalyst, titanomaghemite remains as the main crystalline phase with a minor contribution of metallic iron (~2 wt %) quantified both by Rietveld refinement and the fitting of the experimental PDF (Figure S6).

Catalytic Studies in the Nonoxidative Dehydrogenation of Isobutane. The catalysts were evaluated at 550 °C using an equimolar C_4H_{10}/N_2 mixture (WHSV of 240 mL·h^{-1}·g^{-1} cat) at atmospheric pressure, where the equilibrium conversion of isobutane is ca. 65%. As shown in Figure 6, the activity differs drastically between both monometallic Fe/C_{BTC} and Fe/$C_{MIL\text{-}100}$ systems, much higher for the first one, as initial conversion indicates (61 and 18%, respectively, Figure 6a), but with a dramatically lower selectivity to isobutylene (3 and 91% in the gas phase, respectively, Figure 6b). While the main product is methane (see Table S4), the carbon balance in Fe/C_{BTC} does not even reach 64% (Figure 6c), which is given by a high activity in catalytic cracking and coke formation, resulting in a fast catalyst deactivation during the initial 3 h of reaction. After that, the activity reaches a plateau of conversion and selectivity of around 27 and 26%, respectively. On the other hand, the activity over Fe/$C_{MIL\text{-}100}$ drops during the first hour of reaction reaching a stable conversion in a range close to that of thermal dehydrogenation (see Figure S7) and similar to the activity on commercial Fe_2O_3 nanoparticles ($Ø_{av}$ = 30 nm), with 11% conversion.

There are several possible reasons to explain a high activity in secondary reactions as cracking, hydrogenolysis, isomerization, or coke formation, such as the presence of Brønsted and/or Lewis acid sites on the catalyst surface[6] (for instance, carboxilic groups or low-coordinated iron oxide sites, respectively) or the formation of metallic iron, active for C−C bond cleavage.[19,22] Additionally, metallic iron facilitates the formation of a metastable cementite phase under C_xH_y dehydrogenation conditions, which promotes coke deposition ($Fe_3C \leftrightharpoons \alpha$-Fe + graphite).[47] Accordingly, we speculate that the promotion of Fe/C_{BTC} with potassium may prevent secondary reactions by two possible ways: (i) decreasing surface acidity and/or (ii) stabilizing the iron oxide phase and hindering metallic iron formation.[48,49] The IPA-TPD displayed in Figure S8 suggests a decrease in the Brønsted acidity after

https://doi.org/10.1021/acscatal.1c05303
ACS Catal. 2022, 12, 3832−3844

Table 2. Elemental Analysis of the Spent Catalyst and Coke Estimation

	ICP and CHNS+O/at. %						
catalyst	Fe	Ti, K	C	O	N	H	carbon accumulation[a] ($m_{carbon\ excess}/m_{catalyst}$)
Fe/C_{BTC}	4.8	0	87.1	<0.1	<0.1	7.9	1.22
$K/Fe/C_{BTC}$	5.1	0.3 (K)	85.7	0.9	<0.1	8.1	1.00
$Fe/C_{MIL-100}$	10.4	0	81.5	<0.1	0.1	7.8	0.43
$TiFe/C_{MUV-101}$	7.8	4.6 (Ti)	52.9	18.8	0.3	15.9	0.14

[a]Calculated based on the metal/C ratio prior and after the catalytic tests.

promotion. In fact, the addition of 2 wt % potassium (K_2CO_3) on Fe/C_{BTC} resulted in the stabilization of the catalytic activity at 20% conversion and a selectivity to isobutylene of 89% in the gas phase. This was preceded by an induction period of several hours consisting of both the low carbon balance (ca. 72−81%) and the high selectivity to methane (ca. 85%, initially), which indicates the dominance of side reactions. The promotional effect of potassium has been studied at different K contents, and as shown in Figure 7, the best compromise in terms of activity, selectivity, carbon balance, and induction period has been obtained with 2 wt % potassium, which reveals its limitations as a promoter in this particular case.

As mentioned earlier, the stabilization of the active iron oxide phase under reaction conditions may prevent cracking reactions promoted by metallic iron. The TPR profiles shown in Figure 4 demonstrate enhanced resistance to reduction of the mixed titanomaghemite phase in $TiFe/C_{MUV-101}$, which remains partially stable at 600 °C under a H_2 atmosphere. In fact, the performance of $TiFe/C_{MUV-101}$ shows a high selectivity to isobutylene (above 90%) after a short stabilization period, reaching a stable conversion and selectivity of 28 and 92%, respectively, after more than 8 h of catalytic reaction. Moreover, carbon balance in the gas phase remains stable at ca. 99% in contrast with the low values of 90 and 93% found in Fe/C_{BTC} and $K/Fe/C_{BTC}$, respectively (see Figure 6c).

Finally, to evaluate the catalytic potential of titanium and in particular the role of low-coordinated titanium(IV) sites in the dehydrogenation of isobutane, a commercial TiO_2 (Ø < 25 nm) material was pretreated in hydrogen at 600 °C, following the protocol reported by Li et al. to obtain defective TiO_2,[50] and tested in the dehydrogenation of isobutane. The results displayed in Figure S10 show a relatively low activity of the material under the conditions relevant to this work with an initial conversion of 14% and a selectivity to isobutylene of 85%.

Characterization of Spent Catalysts. The spent catalysts were passivated and analyzed by elemental analysis (see Table 2), which evidences almost total oxygen depletion (<0.1 at. %) in both monometallic Fe/C_{BTC} and $Fe/C_{MIL-100}$ systems, the presence of a small remaining amount in the promoted $K/Fe/C_{BTC}$ catalyst of 0.9 at. %, and the prevalence of 18.8 at. % in $TiFe/C_{MUV-101}$. As already highlighted, this agrees with the stronger resistance of the titanomaghemite phase to reduction under reaction conditions. Second, carbon increased in all the cases not only due to oxygen consumption but also to coke and iron carbide formation. This is clearer when quantifying the carbon excess-to-catalyst mass ratio ($m_{carbon\ excess}/m_{catalyst}$), whose values of 1.22, 1.00, 0.43, and 0.14 in Fe/C_{BTC}, $K/Fe/C_{BTC}$, $Fe/C_{MIL-100}$, and $TiFe/C_{MUV-101}$ indicate a much higher coke formation in the $(K/)Fe/C_{BTC}$ catalysts, duplicating the weight of the catalytic bed. On the other hand, the most active and selective catalyst, $TiFe/C_{MUV-101}$, showed the lower carbon accumulation.

PXRD patterns of the spent catalysts (Figure 8) reveal the characteristic peaks of iron carbide (Fe_3C) in Fe/C_{BTC} and $K/Fe/C_{BTC}$ and graphite in all the cases. Additionally, the presence of metallic iron is observed in Fe/C_{BTC} and $Fe/C_{MIL-100}$ catalysts, with the additional presence of metallic iron for the latter, considering the sharp reflection at 44.7°. The main feature of structured graphite at ca. 26.4° is present in all the cases. Complementarily, the PXRD pattern of the commercial Fe_2O_3 nanoparticles after the reaction was also recorded (see Figure S11), showing the exclusive presence of the iron carbide phase. Concerning the $TiFe/C_{MUV-101}$ catalyst, the fitting of total scattering data in the reciprocal and real space (Figure S6) allowed us to quantify the presence of only 2 wt % cementite (Fe_3C), 23 wt % disordered graphite, and 75 wt % titanomaghemite. The fact that the PDF fit and the Rietveld refinement provide the same phase quantification is a good indication of the reliability of the analysis. The most important conclusion is that the bulk of the $TiFe/C_{MUV-101}$ catalyst remains as an oxide phase over the course of the reaction.

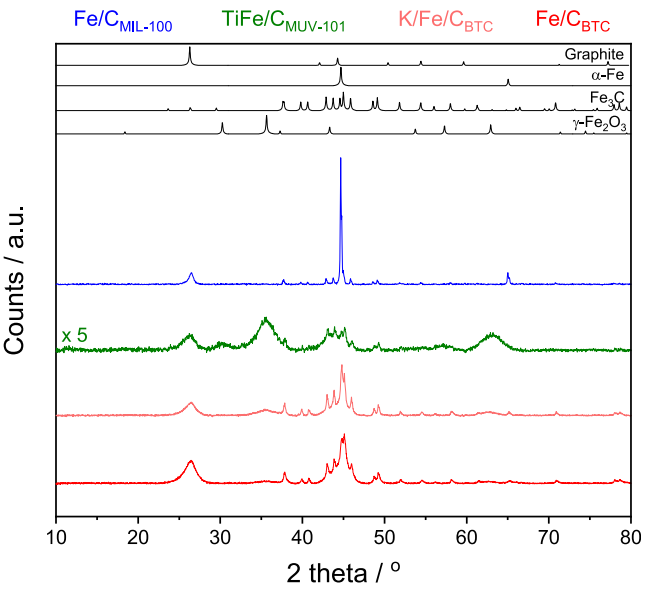

Figure 8. PXRD patterns of the spent catalytic systems: Fe/C_{BTC} (red), $K/Fe/C_{BTC}$ (pale red), $Fe/C_{MIL-100}$ (blue), and $TiFe/C_{MUV-101}$ (green).

To further refine our view of the iron species present on the catalysts' surface under reaction conditions, we have conducted an XPS study of the spent materials (see Figure 9). First, the Fe 2p spectra of Fe/C_{BTC}, $K/Fe/C_{BTC}$, and $Fe/C_{MIL-100}$ show the presence of an intense peak at ca. 706.9 eV of metallic iron or iron carbide, which is not visible in $TiFe/C_{MUV-101}$ (Figure 9a). Furthermore, the detection of Fe^{3+} (ca. 711 eV) in all the catalysts have two possible explanations such as (i) the presence of a thin surface oxide layer even after both

https://doi.org/10.1021/acscatal.1c05303
ACS Catal. 2022, 12, 3832−3844

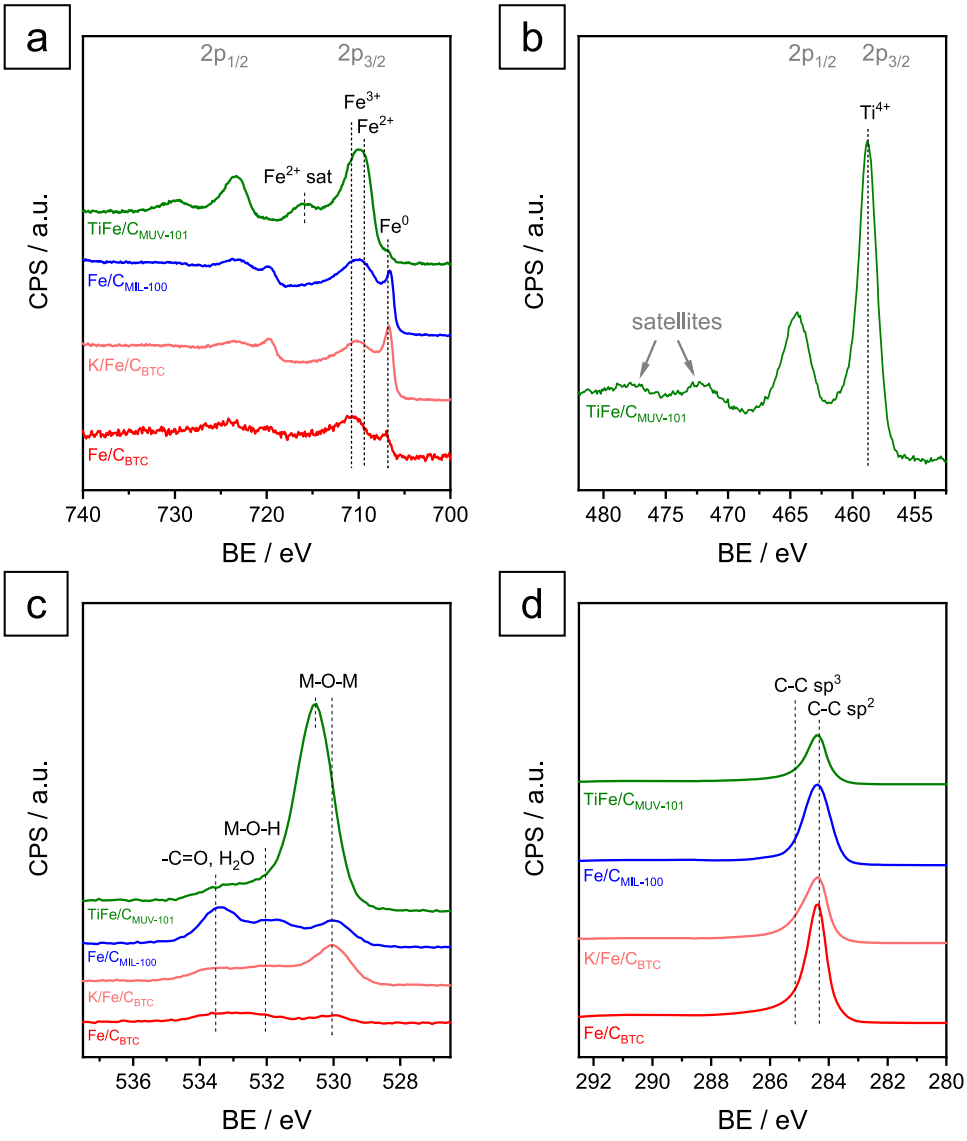

Figure 9. XPS spectra in the Fe 2p (a), Ti 2p (b), O 1s (c), and C 1s (d) regions for the spent catalysts: Fe/C_{BTC} (red), $K/Fe/C_{BTC}$ (pale red), $Fe/C_{MIL\text{-}100}$ (blue), and $TiFe/C_{MUV\text{-}101}$ (green).

prereduction and dehydrogenation processes or (ii) oxygen contamination prior to analysis. Based on the elemental analysis, the first option cannot be discarded since oxygen is detectable in a certain amount in all the samples, although at very low concentration (<0.1 at. %) in both monometallic catalysts. Unlike elemental analysis, sample preparation for the XPS measurement was carried out seeking to avoid contact of the catalyst with air after the catalytic test. However, the high ability of iron to bind oxygen may hardly prevent its oxidation even at very low partial pressure of oxygen, as in the case of the XPS load chamber (P_{O2} = 10^{-5}–10^{-6} Torr). Finally, the component at 709.5 eV together with the satellite at 715.9 eV indicates the prevalence of Fe^{2+} on the $TiFe/C_{MUV\text{-}101}$ catalyst surface. On the other hand, the maximum at 458.8 eV of the Ti 2p signal (Figure 9b) is typically associated with Ti^{4+} in titanium dioxide. The +0.5 eV shift in binding energy compared to the as-prepared $TiFe/C_{MUV\text{-}101}$ catalyst indicates a more oxidized state of titanium under reaction conditions. Interestingly, the Fe/Ti atomic ratio calculated by XPS changes from an initial value of 1.9–2.2 after the catalytic reaction (see Table S5), which may be explained as an effect of iron migration to the catalyst surface after reduction treatment, as shown by *in situ* TEM (Figure 5).

Moreover, the O 1s signals (Figure 9c) show the remnant of M−**O**−M, M−**O**H, and −C=**O**/H_2**O** components but with a very low intensity for all the catalysts except $TiFe/C_{MUV\text{-}101}$, in which the maximum of the component associated with metal oxide shifted from 530.1 to 530.5 eV. This +0.4 eV shift in binding energy has been previously reported in the reduction of Fe^{3+} to Fe^{2+}.[51] Finally, the maximum of the C 1s spectra (Figure 9d) at 284.3 eV with the shoulder at higher binding energy can be associated with sp^2-hybridized carbon (C = C), such as the unsaturated hydrocarbons in coke. Furthermore, oxygenated species are not detectable after the reaction.

Altogether, we could hypothesize that the stabilization of Fe^{2+} species in a system of titanomaghemite nanoparticles (Fe^{3+}, Ti^{4+}), according to the crystallographic data, gives rise to a catalyst certainly active and selective in the dehydrogenation of isobutane to isobutylene. This is in line with the assumption that the formation of a Fe^{2+}/Fe^{3+} tandem is necessary.

https://doi.org/10.1021/acscatal.1c05303
ACS Catal. 2022, 12, 3832−3844

CONCLUSIONS

In this work, we have analyzed the potential application of iron-based MOFs as precursors for the manufacturing of catalysts for the nonoxidative dehydrogenation of isobutane. The pyrolyzed and passivated catalysts were studied *in situ* under reduction and dehydrogenation conditions. Metallic iron has been shown to be highly active in the conversion of isobutane, however promoting secondary reactions and coke accumulation. The later can be promoted from metastable iron carbide, which has shown a poor activity in the dehydrogenation of isobutane.

Two different strategies have been followed to abate secondary reactions: (i) Promotion with potassium improved selectivity to isobutylene, however at the expense of catalytic activity and only moderately decreasing coke formation. Moreover, it required a long induction period to stabilize dehydrogenation activity. On the other hand, (ii) the incorporation of Ti into the active iron phase (from the MUV-101 precursor) led to the stabilization of titanomaghemite nanoparticles, which prevented the formation of undesirable metallic iron under reaction conditions and instead gave rise to the stabilization of Fe^{2+} on the catalyst surface. This resulted in a stable and selective catalyst for several hours on stream with very low formation of coke.

ASSOCIATED CONTENT

Supporting Information

The Supporting Information is available free of charge at https://pubs.acs.org/doi/10.1021/acscatal.1c05303.

Experimental procedures, including powder X-ray diffraction (PXRD), pair distribution function analysis (PDF), transmission electron microscopy (TEM) imaging, annular dark-field scanning transmission electron microscopy (ADF-STEM), electron energy loss spectroscopy (EELS), N_2 physisorption, thermogravimetric analysis (TGA), inductively coupled plasma optical emission spectrometry (ICP-OES), and CHNS +O quantification (PDF)

AUTHOR INFORMATION

Corresponding Author

Jorge Gascon − *KAUST Catalysis Center, Advanced Functional Materials, King Abdullah University of Science and Technology, Thuwal 23955, Saudi Arabia;* orcid.org/0000-0001-7558-7123; Email: jorge.gascon@kaust.edu.sa

Authors

Alberto Rodriguez-Gomez − *KAUST Catalysis Center, Advanced Functional Materials, King Abdullah University of Science and Technology, Thuwal 23955, Saudi Arabia*

Samy Ould-Chikh − *KAUST Catalysis Center, Advanced Functional Materials, King Abdullah University of Science and Technology, Thuwal 23955, Saudi Arabia;* orcid.org/0000-0002-3486-0944

Javier Castells-Gil − *Instituto de Ciencia Molecular, Universitat de València, 46980 Paterna, Spain;* Present Address: School of Chemistry, University of Birmingham, Edgbaston, Birmingham B15 2TT, United Kingdom; orcid.org/0000-0001-7931-3867

Antonio Aguilar-Tapia − *Institut Neel, UPR 2940 CNRS—Université Grenoble Alpes, 38000 Grenoble, France*

Pierre Bordet − *Institut Neel, UPR 2940 CNRS—Université Grenoble Alpes, 38000 Grenoble, France;* orcid.org/0000-0002-1488-2257

Mogbel A. Alrushaid − *Surface Science and Advanced Characterizations Department, SABIC-CRD at KAUST, Thuwal 23955, Saudi Arabia*

Carlos Marti-Gastaldo − *Instituto de Ciencia Molecular, Universitat de València, 46980 Paterna, Spain;* orcid.org/0000-0003-3203-0047

Complete contact information is available at: https://pubs.acs.org/10.1021/acscatal.1c05303

Notes

The authors declare no competing financial interest.

ACKNOWLEDGMENTS

Funding for this work was provided by the King Abdullah University of Science and Technology (KAUST). C.M-G. also thanks the support of Generalitat Valenciana (PROMETEU/2021/054), Gobierno de España (PID2020-118117RB-I00) and the Maria de Maeztu Units of Excellence Programme (CEX-2019-000919-M). We also thank Julian Vittenet and Diego Mateo for technical support and Sandra Ramirez Cherbury for artwork.

REFERENCES

(1) Vogt, E. T. C.; Weckhuysen, B. M. Fluid catalytic cracking: recent developments on the grand old lady of zeolite catalysis. *Chem. Soc. Rev.* **2015**, *44*, 7342−7370.

(2) Corma, A.; Corresa, E.; Mathieu, Y.; Sauvanaud, L.; Al-Bogami, S.; Al-Ghrami, M. S.; Bourane, A. Crude oil to chemicals: light olefins from crude oil. *Catal. Sci. Technol.* **2017**, *7*, 12−46.

(3) Alabdullah, M. A.; Gomez, A. R.; Vittenet, J.; Bendjeriou-Sedjerari, A.; Xu, W.; Abba, I. A.; Gascon, J. A Viewpoint on the Refinery of the Future: Catalyst and Process Challenges. *ACS Catal.* **2020**, *10*, 8131−8140.

(4) Butadiene/Butylenes. *PERP 09/10-5, Chemsystems PERP Program*; Nexant: White Plains, NY, 2012.

(5) Shi, L.; Wang, Y.; Yan, B.; Song, W.; Shao, D.; Lu, A.-H. Progress in selective oxidative dehydrogenation of light alkanes to olefins promoted by boron nitride catalysts. *Chem. Commun.* **2018**, *54*, 10936−10946.

(6) Sattler, J. J. H. B.; Ruiz-Martinez, J.; Santillan-Jimenez, E.; Weckhuysen, B. M. Catalytic Dehydrogenation of Light Alkanes on Metals and Metal Oxides. *Chem. Rev.* **2014**, *114*, 10613−10653.

(7) Otroshchenko, T.; Jiang, G.; Kondratenko, V. A.; Rodemerck, U.; Kondratenko, E. V. Current status and perspectives in oxidative, non-oxidative and CO_2-mediated dehydrogenation of propane and isobutane over metal oxide catalysts. *Chem. Soc. Rev.* **2021**, *50*, 473−527.

(8) Langeslay, R. R.; Kaphan, D. M.; Marshall, C. L.; Stair, P. C.; Sattelberger, A. P.; Delferro, M. Catalytic Applications of Vanadium: A Mechanistic Perspective. *Chem. Rev.* **2019**, *119*, 2128−2191.

(9) Rodemerck, U.; Sokolov, S.; Stoyanova, M.; Bentrup, U.; Linke, D.; Kondratenko, E. V. Influence of support and kind of VO_x species on isobutene selectivity and coke deposition in non-oxidative dehydrogenation of isobutane. *J. Catal.* **2016**, *338*, 174−183.

(10) Rodriguez-Gomez, A.; Chowdhury, A. D.; Caglayan, M.; Bau, J. A.; Abou-Hamad, E.; Gascon, J. Non-oxidative dehydrogenation of isobutane over supported vanadium oxide: nature of the active sites and coke formation. *Catal. Sci. Technol.* **2020**, *10*, 6139−6151.

(11) Tian, Y.-P.; Bai, P.; Liu, S.-M.; Liu, X.-M.; Yan, Z.-F. VO_x−K_2O/γ-Al_2O_3 catalyst for nonoxidative dehydrogenation of isobutane. *Fuel Process. Technol.* **2016**, *151*, 31−39.

(12) Mu, J.; Shi, J.; France, L. J.; Wu, Y.; Zeng, Q.; Liu, B.; Jiang, L.; Long, J.; Li, X. Hybrid Mo−CT Nanowires as Highly Efficient

Catalysts for Direct Dehydrogenation of Isobutane. *ACS Appl. Mater. Interfaces* **2018**, *10*, 23112−23121.
(13) Zhao, H.; Song, H.; Chou, L.; Zhao, J.; Yang, J.; Yan, L. Insight into the structure and molybdenum species in mesoporous molybdena−alumina catalysts for isobutane dehydrogenation. *Catal. Sci. Technol.* **2017**, *7*, 3258−3267.
(14) Zhang, Y.; Zhao, Y.; Otroshchenko, T.; Han, S.; Lund, H.; Rodemerck, U.; Linke, D.; Jiao, H.; Jiang, G.; Kondratenko, E. V. The effect of phase composition and crystallite size on activity and selectivity of ZrO_2 in non-oxidative propane dehydrogenation. *J. Catal.* **2019**, *371*, 313−324.
(15) Otroshchenko, T. P.; Kondratenko, V. A.; Rodemerck, U.; Linke, D.; Kondratenko, E. V. Non-oxidative dehydrogenation of propane, n-butane, and isobutane over bulk ZrO_2-based catalysts: effect of dopant on the active site and pathways of product formation. *Catal. Sci. Technol.* **2017**, *7*, 4499−4510.
(16) Schreiber, M. W.; Plaisance, C. P.; Baumgärtl, M.; Reuter, K.; Jentys, A.; Bermejo-Deval, R.; Lercher, J. A. Lewis−Brønsted Acid Pairs in Ga/H-ZSM-5 To Catalyze Dehydrogenation of Light Alkanes. *J. Am. Chem. Soc.* **2018**, *140*, 4849−4859.
(17) Matveyeva, A. N.; Zaitseva, N. A.; Mäki-Arvela, P.; Aho, A.; Bachina, A. K.; Fedorov, S. P.; Murzin, D. Y.; Pakhomov, N. A. Fluidized-Bed Isobutane Dehydrogenation over Alumina-Supported Ga_2O_3 and Ga_2O_3−Cr_2O_3 Catalysts. *Ind. Eng. Chem. Res.* **2018**, *57*, 927−938.
(18) Chen, M.; Wu, J.-L.; Liu, Y.-M.; Cao, Y.; Guo, L.; He, H.-Y.; Fan, K.-N. Study in support effect of In_2O_3/MO_x (M=Al, Si, Zr) catalysts for dehydrogenation of propane in the presence of CO_2. *Appl. Catal., A* **2011**, *407*, 20−28.
(19) Hu, B.; Schweitzer, N. M.; Zhang, G. H.; Kraft, S. J.; Childers, D. J.; Lanci, M. P.; Miller, J. T.; Hock, A. S. Isolated Fe-II on Silica As a Selective Propane Dehydrogenation Catalyst. *ACS Catal.* **2015**, *5*, 3494−3503.
(20) Tan, S.; Hu, B.; Kim, W. G.; Pang, S. H.; Moore, J. S.; Liu, Y. J.; Dixit, R. S.; Pendergast, J. G.; Sholl, D. S.; Nair, S.; Jones, C. W. Propane Dehydrogenation over Alumina-Supported Iron/Phosphorus Catalysts: Structural Evolution of Iron Species Leading to High Activity and Propylene Selectivity. *ACS Catal.* **2016**, *6*, 5673−5683.
(21) Cheng, M.; Zhao, H. H.; Yang, J.; Zhao, J.; Yan, L.; Song, H. L.; Chou, L. J. Synthesis and Catalytic Performance of a Dual-Sites Fe-Zn Catalyst Based on Ordered Mesoporous Al_2O_3 for Isobutane Dehydrogenation. *Catal. Lett.* **2019**, *149*, 1326−1336.
(22) Sun, Y. A.; Wu, Y. M.; Shan, H. H.; Wang, G. W.; Li, C. Y. Studies on the promoting effect of sulfate species in catalytic dehydrogenation of propane over Fe_2O_3/Al_2O_3 catalysts. *Catal. Sci. Technol.* **2015**, *5*, 1290−1298.
(23) Sarazen, M. L.; Jones, C. W. MOF-Derived Iron Catalysts for Nonoxidative Propane Dehydrogenation. *J. Phys. Chem. C* **2018**, *122*, 28637−28644.
(24) Yun, J. H.; Lobo, R. F. Catalytic dehydrogenation of propane over iron-silicate zeolites. *J. Catal.* **2014**, *312*, 263−270.
(25) Shimada, H.; Akazawa, T.; Ikenaga, N.; Suzuki, T. Dehydrogenation of isobutane to isobutene with iron-loaded activated carbon catalyst. *Appl. Catal., A* **1998**, *168*, 243−250.
(26) Boot, L. A.; van Dillen, A. J.; Geus, J. W.; van Buren, F. R. Iron-Based Dehydrogenation Catalysts Supported on Zirconia. II. The Behavior in the Dehydrogenation of 1-Butene. *J. Catal.* **1996**, *163*, 195−203.
(27) Stobbe, D. E.; van Buren, F. R.; Hoogenraad, M. S.; van Dillen, A. J.; Geus, J. W. Iron oxide dehydrogenation catalysts supported on magnesium oxide. Part 3.—But-1-ene dehydrogenation activity. *J. Chem. Soc., Faraday Trans.* **1991**, *87*, 1639−1647.
(28) Longbottom, R. J.; Ostrovski, O.; Zhang, J.; Young, D. Stability of Cementite Formed from Hematite and Titanomagnetite Ore. *Metall. Mater. Trans. B* **2007**, *38*, 175−184.
(29) Santos, V. P.; Wezendonk, T. A.; Jaén, J. J. D.; Dugulan, A. I.; Nasalevich, M. A.; Islam, H.-U.; Chojecki, A.; Sartipi, S.; Sun, X.; Hakeem, A. A.; Koeken, A. C. J.; Ruitenbeek, M.; Davidian, T.; Meima, G. R.; Sankar, G.; Kapteijn, F.; Makkee, M.; Gascon, J. Metal organic framework-mediated synthesis of highly active and stable Fischer-Tropsch catalysts. *Nat. Commun.* **2015**, *6*, No. 6451.
(30) Sun, X.; Suarez, A. I. O.; Meijerink, M.; van Deelen, T.; Ould-Chikh, S.; Zečević, J.; de Jong, K. P.; Kapteijn, F.; Gascon, J. Manufacture of highly loaded silica-supported cobalt Fischer−Tropsch catalysts from a metal organic framework. *Nat. Commun.* **2017**, *8*, No. 1680.
(31) Wang, R.; Haspel, H.; Pustovarenko, A.; Dikhtiarenko, A.; Russkikh, A.; Shterk, G.; Osadchii, D.; Ould-Chikh, S.; Ma, M.; Smith, W. A.; Takanabe, K.; Kapteijn, F.; Gascon, J. Maximizing Ag Utilization in High-Rate CO_2 Electrochemical Reduction with a Coordination Polymer-Mediated Gas Diffusion Electrode. *ACS Energy Lett.* **2019**, *4*, 2024−2031.
(32) Bavykina, A.; Kolobov, N.; Khan, I. S.; Bau, J. A.; Ramirez, A.; Gascon, J. Metal−Organic Frameworks in Heterogeneous Catalysis: Recent Progress, New Trends, and Future Perspectives. *Chem. Rev.* **2020**, *120*, 8468−8535.
(33) Castells-Gil, J.; Ould-Chikh, S.; Ramírez, A.; Ahmad, R.; Prieto, G.; Gómez, A. R.; Garzon-Tovar, L.; Telalovic, S.; Liu, L.; Genovese, A.; Padial, N. M.; Aguilar-Tapia, A.; Bordet, P.; Cavallo, L.; Martí-Gastaldo, C.; Gascon, J. Unlocking mixed oxides with unprecedented stoichiometries from heterometallic metal-organic frameworks for the catalytic hydrogenation of CO_2. *Chem. Catal.* **2021**, *1*, 364−382.
(34) Wezendonk, T. A.; Sun, X.; Dugulan, A. I.; van Hoof, A. J. F.; Hensen, E. J. M.; Kapteijn, F.; Gascon, J. Controlled formation of iron carbides and their performance in Fischer-Tropsch synthesis. *J. Catal.* **2018**, *362*, 106−117.
(35) Ramirez, A.; Gevers, L.; Bavykina, A.; Ould-Chikh, S.; Gascon, J. Metal Organic Framework-Derived Iron Catalysts for the Direct Hydrogenation of CO_2 to Short Chain Olefins. *ACS Catal.* **2018**, *8*, 9174−9182.
(36) Castells-Gil, J.; M Padial, N.; Almora-Barrios, N.; Gil-San-Millán, R.; Romero-Ángel, M.; Torres, V.; da Silva, I.; Vieira, B. C. J.; Waerenborgh, J. C.; Jagiello, J.; Navarro, J. A. R.; Tatay, S.; Martí-Gastaldo, C. Heterometallic Titanium-Organic Frameworks as Dual-Metal Catalysts for Synergistic Non-buffered Hydrolysis of Nerve Agent Simulants. *Chem* **2020**, *6*, 3118−3131.
(37) García-Martínez, J.; Li, K. *Mesoporous Zeolites Preparation, Characterization and Applications*; Wiley-VCH: Weinheim, 2015.
(38) Fujii, T.; de Groot, F. M. F.; Sawatzky, G. A.; Voogt, F. C.; Hibma, T.; Okada, K. In situ XPS analysis of various iron oxide films grown by NO_2-assisted molecular-beam epitaxy. *Phys. Rev. B* **1999**, *59*, 3195−3202.
(39) Grosvenor, A. P.; Kobe, B. A.; Biesinger, M. C.; McIntyre, N. S. Investigation of multiplet splitting of Fe 2p XPS spectra and bonding in iron compounds. *Surf. Interface Anal.* **2004**, *36*, 1564−1574.
(40) Biesinger, M. C.; Payne, B. P.; Grosvenor, A. P.; Lau, L. W. M.; Gerson, A. R.; Smart, R. S. C. Resolving surface chemical states in XPS analysis of first row transition metals, oxides and hydroxides: Cr, Mn, Fe, Co and Ni. *Appl. Surf. Sci.* **2011**, *257*, 2717−2730.
(41) Idczak, K.; Idczak, R.; Konieczny, R. An investigation of the corrosion of polycrystalline iron by XPS, TMS and CEMS. *Phys. B* **2016**, *491*, 37−45.
(42) Biesinger, M. C.; Lau, L. W. M.; Gerson, A. R.; Smart, R. S. C. Resolving surface chemical states in XPS analysis of first row transition metals, oxides and hydroxides: Sc, Ti, V, Cu and Zn. *Appl. Surf. Sci.* **2010**, *257*, 887−898.
(43) Database, N. X.-r. P. S. *NIST Standard Reference Database Number 20*; National Institute of Standards and Technology: Gaithersburg, MD, 2000.
(44) Wu, W.; Xiao, X.; Zhang, S.; Ren, F.; Jiang, C. Facile method to synthesize magnetic iron oxides/TiO_2 hybrid nanoparticles and their photodegradation application of methylene blue. *Nanoscale Res. Lett.* **2011**, *6*, No. 533.
(45) Perkas, N.; Palchik, O.; Brukental, I.; Nowik, I.; Gofer, Y.; et al. A Mesoporous Iron−Titanium Oxide Composite Prepared Sonochemically. *J. Phys. Chem. B* **2003**, *107*, 8772−8778.

https://doi.org/10.1021/acscatal.1c05303
ACS Catal. 2022, 12, 3832−3844

(46) Tung, W. S.; Daoud, W. A. New Approach Toward Nanosized Ferrous Ferric Oxide and Fe_3O_4-doped Titanium Dioxide Photocatalysts. *ACS Appl. Mater. Interfaces* **2009**, *1*, 2453−2461.
(47) Chipman, J. Thermodynamics and phase diagram of the Fe-C system. *Metall. Mater. Trans. B* **1972**, *3*, 55−64.
(48) Ndlela, S. C.; Shanks, B. H. Reducibility of Potassium-Promoted Iron Oxide under Hydrogen Conditions. *Ind. Eng. Chem. Res.* **2003**, *42*, 2112−2121.
(49) Russkikh, A.; Shterk, G.; Al-Solami, B. H.; Fadhel, B. A.; Ramirez, A.; Gascon, J. Turning Waste into Value: Potassium-Promoted Red Mud as an Effective Catalyst for the Hydrogenation of CO_2. *ChemSusChem* **2020**, *13*, 2981−2987.
(50) Li, C.-F.; Guo, X.; Shang, Q.-H.; Yan, X.; Ren, C.; Lang, W.-Z.; Guo, Y.-J. Defective TiO_2 for Propane Dehydrogenation. *Ind. Eng. Chem. Res.* **2020**, *59*, 4377−4387.
(51) Deng, X.; Lee, J.; Matranga, C. Preparation and characterization of Fe_3O_4(111) nanoparticles and thin films on Au(111). *Surf. Sci.* **2010**, *604*, 627−632.

https://doi.org/10.1021/acscatal.1c05303
ACS Catal. 2022, 12, 3832−3844